Article:
McClelland, I. orcid.org/0000-0001-9821-715X, Booth, S.G. orcid.org/0000-0001-7643-4196, El-Shinawi, H. orcid.org/0000-0002-4743-5576 et al. (6 more authors) (2021) In situ diffusion measurements of a NASICON-structured all-solid-state battery using muon spin relaxation. ACS Applied Energy Materials, 4 (2). pp. 1527-1536.

https://doi.org/10.1021/acsaem.0c02722

ACS APPLIED ENERGY MATERIALS

www.acsaem.org Article

In Situ Diffusion Measurements of a NASICON-Structured All-Solid-State Battery Using Muon Spin Relaxation

Innes McClelland, Samuel G. Booth, Hany El-Shinawi, Beth I. J. Johnston, Jasmin Clough, Weimin Guo, Edmund J. Cussen, Peter J. Baker, and Serena A. Corr*

Cite This: *ACS Appl. Energy Mater.* 2021, 4, 1527−1536 Read Online

ACCESS | Metrics & More | Article Recommendations | Supporting Information

ABSTRACT: In situ muon spin relaxation is demonstrated as an emerging technique that can provide a volume-averaged local probe of the ionic diffusion processes occurring within electrochemical energy storage devices as a function of state of charge. Herein, we present work on the conceptually interesting NASICON-type all-solid-state battery $LiM_2(PO_4)_3$, using M = Ti in the cathode, M = Zr in the electrolyte, and a Li metal anode. The pristine materials are studied individually and found to possess low ionic hopping activation energies of ∼50−60 meV and competitive Li^+ self-diffusion coefficients of $\sim 10^{-10}-10^{-9}$ cm^2 s^{-1} at 336 K. Lattice matching of the cathode and electrolyte crystal structures is employed for the all-solid-state battery to enhance Li^+ diffusion between the components in an attempt to minimize interfacial resistance. The cell is examined by in situ muon spin relaxation, providing the first example of such ionic diffusion measurements. This technique presents an opportunity to the materials community to observe intrinsic ionic dynamics and electrochemical behavior simultaneously in a nondestructive manner.

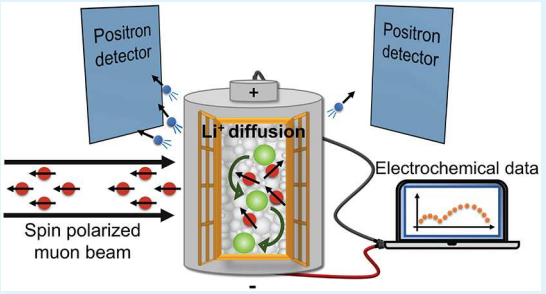

KEYWORDS: *muon spin relaxation, solid-state battery, nondestructive technique, Li^+ diffusion*

INTRODUCTION

As the electric vehicle market expands rapidly, the social and economic importance of improved energy storage devices grows concurrently, thus proving vital the utilization of next-generation technologies such as solid-state-batteries (SSBs).[1] The benefits of SSBs are well-established: increased safety (removal of flammable organic solvent), an enhanced potential window, extended cycle life and stability against a Li metal anode.[2−5] However, serious challenges, such as large interfacial resistances, scalability, chemical stability, low ionic conductivity, and dendritic growth remain prevalent.[6−9] Material development remains crucial and commercial uptake demands SSBs possessing excellent ionic diffusivity through the bulk and across chemically stable interfaces between the components to function efficiently.

Problematic tendencies of SSBs include abrupt short-circuits during cycling, regularly manifested through electrolyte cracking or inadequate electrode wetting which can lead to the deterioration of electrical contact. These mechanisms are linked to electrode volume change on charge/discharge which can induce significant internal strain, especially at interfaces.[10,11] Deleterious interfacial strain has previously been linked to increased resistances and capacity fade and has also been known to increase with variable current densities and at certain discharge states within SSBs.[12,13] Indeed, poor electrical contact caused by interfacial strain often accentuates an uneven current distribution which can expedite a short-circuit.[2,14] On the cathode/electrolyte boundary, methods such as lattice matching,[15] which involve pairing structurally similar electrolytes/electrodes, have been employed in an attempt to harmonize ionic diffusion pathways across interfacial regions and minimize resistance,[16] while thin buffer layers have been used for the anode/electrolyte boundary.[17] Control over both the anode and cathode interfacial areas is crucial for battery performance; especially for long-term cyclability.[15,17] A further challenge for solid electrolytes is that of ionic conductivity, a process generally governed by defect/vacancy concentration and distribution. Diffusion is often hindered by rigid crystalline electrolytes and consequently slower ionic conductivities are commonplace in comparison to liquid electrolytes.[2,4,18]

Ceramic NASICON-structured $LiZr_2(PO_4)_3$ (LZP) has been investigated previously as a potential solid-state electrolyte due to its fast ionic conductivity, high upper working voltage limit (up to 5.5 V vs Li^+/Li), and air stability.[17,19] The phosphate structure provides an open three-dimensional diffusion framework with large cavity sizes which can enhance Li^+ mobility.[20−22] However, difficulties using conventional

Received: November 2, 2020
Accepted: January 11, 2021
Published: January 21, 2021

https://dx.doi.org/10.1021/acsaem.0c02722
ACS Appl. Energy Mater. 2021, 4, 1527−1536

sintering methods to obtain dense forms of the fast ionically conducting α-type phase at room temperature have limited progression.[15] LZP possesses complex polymorphism: only the stabilized rhombohedral α-type phase (space group $R\bar{3}c$) and not the β-type polymorph is suitable for use as a solid electrolyte, displaying ionic conductivities of $\geq 1 \times 10^{-4}$ S cm^{-1}.[15,17,23] The triclinic α-type phase (space group $C\bar{1}$), which is generally present at room temperature displays low ionic conductivities ($\approx 10^{-8}$ S cm^{-1}), only transitioning to the rhombohedral phase at around 50 °C.[24] Within the rhombohedral phase, Li^+ occupies disordered tetrahedral 36f sites located near 6b (M1) sites, with Li^+ conduction occurring via hops between these sites.[21] It was previously believed that only a single 36f site around a 6b site was occupied by a Li atom; however, Noda et al. have recently shown that double occupancy is possible when both Li^+ ions locate further from the center of the 6b site and that diffusion occurs via a pushing-out and repulsion mechanism.[19]

Dopant atoms, such as Ti, Ge, and Al, have been previously used to stabilize the rhombohedral phase at room temperature and enhance ionic conductivity, yet often do so at the expense of enlarged interfacial impedances because of the reducible oxidation state of some of the doped cations against Li metal.[25−29] Dopants have also been reported to increase interfacial resistances between the cathode and electrolyte, and therefore, their avoidance is preferable for lattice matching.[16] When LZP is placed in contact with Li metal, a passivating interphase consisting of Li_3P and Li_8ZrO_6 forms and the stable oxidation state of the Zr^{4+} cation against this layer provides chemical stability.[5,15,30] $LiTi_2(PO_4)_3$ (LTP) offers an improved Li^+ ion conductivity over LZP as a consequence of the suitability of the diffusion channels provided by Ti's apt ionic radius (the ionic radii of Ti^{4+} and Zr^{4+} are 60.5 and 72.0 pm, respectively), which permits facile Li^+ movement along the M1-M2-M1 channel.[22,25,31,32] However, the reactivity of LTP against Li metal combined with the variable Ti^{3+}/Ti^{4+} redox couple suggests suitability as an electrode material.[15,19]

Muon spin relaxation spectroscopy (μSR) implants spin-polarized, positively charged muons within a target material to act as a local probe.[33] Once embedded, the evolution of the muon spin direction is affected by any magnetic fields it experiences, before decaying with an average lifetime of 2.2 μs into two neutrinos and a positron. Importantly, the positron is emitted preferentially along the direction of the muon spin at the time of decay. The magnetic environment, which influences the muon spin, includes any externally applied magnetic field, the fluctuating electronic fields from present paramagnetic ions, and any nuclear dipole fields present within the sample, both static and dynamic. Thus, muons probe ionic fluctuations on a length-scale of only a few unit cells and at a time-scale dependent on the frequency of Larmor precession due to the magnetic field they experience. By following the time-dependent progression of the count rate asymmetry of daughter positrons, A(t), between detectors on opposite sides of the sample, the muon's local magnetic environment can be inferred. The externally applied magnetic field can be used to isolate the contribution to the received signal from any moving nuclear dipole fields of diffusing species, and consequently, key ionic diffusion parameters can be elucidated.[33,34] μSR has been proven as a reliable and reproducible probe of the mobility of various ions (such as Li^+, Na^+, and I^-) on a time scale of 10^{-5}−10^{-8} s.[35−47] Given recent successes on the study of isolated materials, the possibility of in situ diffusion measurements using μSR represents an enticing opportunity to directly track ionic dynamics within batteries as a function of state of charge. Furthermore, the nondestructive nature of the technique means that intrinsic material properties and electrochemical behavior can be followed simultaneously without interference. This microscopic insight can be coupled with complementary macroscopic information from various electrochemical techniques to link phenomena observed from multiple viewpoints to the performance of functioning cells.

Herein, we report on the diffusion characteristics of pristine LZP and LTP using nondestructive temperature dependent muon spin relaxation (μSR). We also report, for the first time, the use of in situ μSR to follow the diffusivity behavior within the solid electrolyte of an all-solid-state Li|LZP|LTP cell as a function of discharge voltage, reaching low potentials to follow the point of cell failure.

EXPERIMENTAL SECTION

Synthesis and Characterization. LZP, LTP, and an Li|LZP|LTP solid-state battery cell were synthesized and prepared using the procedures described previously by our group and El-Shinawi et al.[15,48] High calcination temperatures of 1100 °C for 50 min and rapid quenching to room temperature were used to obtain pure α-type phase LZP. LTP was synthesized using a similar sol−gel procedure to LZP, but lower calcination temperatures of 550 °C and an increased dwell time of 24 h were employed. Powder X-ray diffraction (PXRD) characterization of the samples was performed using a Rigaku Miniflex diffractometer in reflection mode using Cu Kα radiation. Electrochemical measurements were performed using a BioLogic VSP potentiostat. Electrochemical impedance spectroscopy measurements were carried out within a frequency range of 1 MHz to 1 Hz. The Li|LZP|LTP cell was assembled and sealed at 1.5 bar within a CR2016 MTI coin cell with a 10 mm diameter Kapton inspection window. The cosintered electrolyte/cathode pellet with a diameter of 13 mm was modified via polishing using papers with grit numbers from 400 to 2500 to a final thickness of 1.0 mm. VESTA was used to create unit cell depictions.[49]

Muon Spectroscopy. μSR measurements were completed on the EMU beamline at the ISIS Pulsed Neutron and Muon Source. Powder samples (~1 g) of LZP and LTP were transferred into Ti sample holders with a thin Ti foil window to allow muon implantation. Spin-polarized positive muons of initial energy 4.12 MeV were implanted into the samples to act as a probe of Li^+ diffusion. Muons were implanted with a controllable penetration range of between 0.1−1.0 mm, and after rapid thermalization, they preferentially stop at electronegative interstitial sites in the crystal structure, commonly near oxygen. Thin Ag foil was used in front of the cell as a beam degrader when necessary to control the penetration depth. Applied longitudinal magnetic fields were used to decouple the muon spin from its surrounding local nuclear moments. Measurements were performed in 0, 5, and 10 G longitudinal fields, along with 100 G transverse field calibration runs. A temperature range of 100−400 K was measured, encapsulating a low temperature baseline and the thermally activated region, where Li^+ ions overcome the energetic barriers opposing ionic transport. The beam spot has a roughly Gaussian profile, and its size was collimated to optimize the rate of data collection and minimize background noise. Data fitting was completed using Mantid software package.[50]

In Situ Cell Holder. A custom-built holder to house the coin cell was designed in collaboration with the ISIS Neutron and Muon Source. A cell was placed inside the adapted holder design, and the inspection windows were aligned to allow muon implantation. Teflon screws were used to tighten the holder and secure the cell while ensuring electrical isolation between terminals. An Ag mask was included on the front of the holder to stop any wayward muons that were not incident on the inspection window. Ag (similar to Ti, which is used for the powder sample holders) has a very small nuclear

https://dx.doi.org/10.1021/acsaem.0c02722
ACS Appl. Energy Mater. 2021, 4, 1527−1536

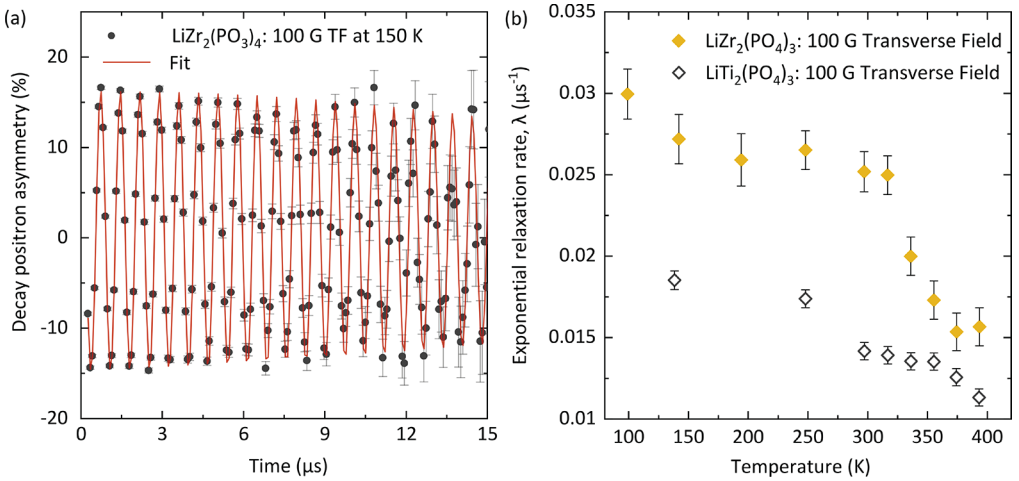

Figure 1. (a) μSR measurement of solid electrolyte LZP in a 100 G applied transverse field at 150 K. (b) Temperature-dependent relaxation rate λ obtained via fitting of an oscillating exponential decay function to transverse field data.

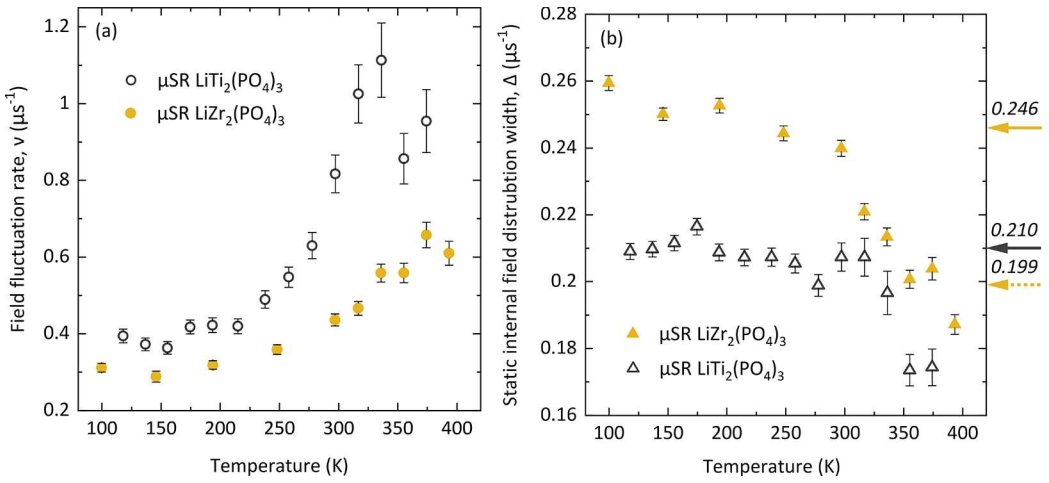

Figure 2. μSR measurement of (a) the field fluctuation rate ν, which is directly analogous to the ionic jump frequency and (b) the static field distribution width Δ of the implanted muons within LZP and LTP. Computationally predicted Δ values are shown on the opposite y axis as a yellow arrow for triclinic LZP, a black arrow for LTP, and a dotted yellow arrow for rhombohedral LZP.

magnetic moment, meaning the signal from any muons implanted within the mask itself could be subtracted as background.

RESULTS AND DISCUSSION

$LiTi_2(PO_4)_3$ and $LiZr_2(PO_4)_3$. $LiTi_2(PO_4)_3$ (LTP) and $LiZr_2(PO_4)_3$ (LZP) were synthesized by an unmodified sol–gel method.[15,48] Prepared LZP contained only the α-type polymorph, with primarily the triclinic phase present at room temperature, as expected (Figure S1). For LZP, the triclinic phase is known to go through a phase transition to the conductive rhombohedral phase around 50 °C.[15] LTP does not undergo a phase change in this temperature range and exists in a rhombohedral structure of space group $R\bar{3}c$.

A fitted 100 G transverse field μSR measurement for LZP is displayed in Figure 1a, showing the rapid change in the asymmetry of positron detection as the muon spin precesses around the applied field, which is much stronger than any internal field of nuclear or electronic origin. Fitting multiple oscillation functions reveals that all muons precess at the Larmor frequency of a free muon in an applied field 135.5 MHz T^{-1}. The low ionic dynamics at 150 K and the lack of unpaired electron spins mean that the asymmetry envelope takes a relatively flat form with little relaxation. Similar data were observed for the cathode LTP (Figure S2). Consequently, no relaxation component was used in the longitudinal field data analysis. To confirm this quantitatively, transverse field data were modeled using a background component and an oscillating exponential relaxation with rate λ, shown in Figure 1. Both materials exhibit low λ values; the flat regions at low temperatures indicate a static environment while the subsequent decrease is a consequence of dynamical field fluctuations above 300 K, indicating the onset of Li^+ diffusion. This occurs at a lower temperature of between 250–300 K for cathode LTP. The larger drop in λ for LZP is likely due to the phase change from triclinic to rhombohedral around 320 K, which will alter the spatial distribution of muon stopping sites.

Longitudinal field (0, 5, and 10 G) experiments were also applied, for which the dynamical field fluctuations created by the nuclear dipole of Li^+ hopping between crystal sites causes a spin flip via the absorption of energy by the muon spin Zeeman levels.[51] Longitudinal field data were fit using a flat background component, and the dynamical form of the Kubo–Toyabe function described as

https://dx.doi.org/10.1021/acsaem.0c02722
ACS Appl. Energy Mater. 2021, 4, 1527–1536

$$A_0P(t) = A_{bg} + A_{KT}P_{KT}(\Delta, \nu, t) \quad (1)$$

where A_{bg} and A_{KT} are the respective amplitudes of the two components. P_{KT} represents the dynamic Kubo−Toyabe function, which is sensitive to the trend of the static field distribution width (Δ) and the field fluctuation rate (ν) with time.[52] The field fluctuation rate offers information on any dynamical fields felt by the muons, which most likely arise from diffusing Li^+. Hence, ν is analogous to the ionic hopping rate.[34]

A longitudinal field strength of 10 G was found sufficient to retain muon spin polarization by quenching the relaxation contribution from nearby nuclear magnetic moments and broadly align the spin along the direction of the applied field (Figures S3 and S4). Constraining the Kubo−Toyabe function to three applied field strengths provided an accurate model by isolating the contribution to the asymmetry signal from Li^+ hopping. Given that LZP is an excellent insulator and that relatively small initial asymmetry values were observed (Figure S3), an appreciable fraction of implanted muons may pick up an electron to form a muonium state (μ^+e^-).[53] This manifests in the data as an exponential decay in an early time domain from a rapidly relaxing muonium signal. To combat this effect, early time domain points were discarded, and the data were fit in a time range of 1−25 μs for LZP. The onset of Li^+ diffusion is seen to occur at around 300 K for the electrolyte LZP and 250 K for the cathode LTP, in agreement with the transverse field data in both instances. Above these temperatures, ν increases rapidly with temperature as Li^+ becomes increasingly mobile. The high temperature drop in ν for LTP can be explained by the Li^+ dynamics becoming too fast to be probed effectively: an effect commonly seen in μSR.[36,46]

Figure 2b displays the temperature dependence of Δ, defined as the width of the static distribution of magnetic fields experienced by the muons, primarily decided by the proximity and strength of nearby nuclear dipole fields. The increased value of Δ for LZP can be attributed to the larger nuclear magnetic moment of the Zr^{4+} cation in comparison to Ti^{4+}.[54] Both samples exhibit a relatively constant value or a slight decrease, before a sharper drop is seen at high temperatures. This is a consequence of a motional narrowing effect: as Li^+ ions begin to diffuse rapidly, their nuclear fields increasingly differ throughout the structure and thus their contribution to Δ is lowered.[46] The larger decrease observed for LZP may be explained by the phase change from triclinic to rhombohedral at around 320 K as the spatial arrangement of muon stopping sites is altered. To distinguish between the effects on Δ of the structural transition in LZP and potential motional narrowing, Δ was calculated and averaged over a selection of potential muon stopping sites in each material, for which details can be found in Tables S1−S6. Very good agreement with the data was found for potential muon sites approximately 1 Å from an oxygen site, similar to the length of an O−H bond (~0.97 Å).[55] From the calculations, Δ is predicted to decrease from 0.246 to 0.199 μs^{-1} with the phase change in LZP. These results show that the different Δ values observed experimentally all relate to common muon stopping sites and that the structural transition dominates the change seen in LZP, rather than the motional narrowing which is also evident. Δ was also predicted as around 0.210 μs^{-1} at potential muon stopping sites in LTP, matching well with experimental values.

An Arrhenius analysis of the temperature dependence of ν was completed to yield an activation energy barrier E_A for Li^+ diffusion (Figure 3). This was extracted for LZP (electrolyte) and LTP (cathode) as around 51 ± 8 and 63 ± 6 meV,

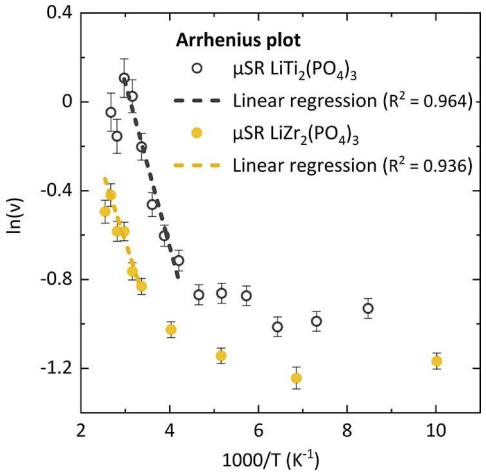

Figure 3. Arrhenius plot of the logarithm of the field fluctuation rate ν against reciprocal temperature for both LZP and LTP. Only the thermally activated region of both materials (300−380 K for LZP and 240−340 K for LTP) was fitted by a linear regression which is shown as a dotted line.

respectively. In comparison to other solid electrolyte materials investigated using μSR, these values are lower than for garnet structured materials (≈200 meV), comparable to sulfide electrolyte material $Li_{10}GeP_2S_{12}$ (≈90 meV), and very similar to many cathode materials.[35−37,39,40,53,56−58] It is worth noting that μSR is a volume-averaged probe, meaning intragrain diffusion mechanisms will dominate the signal. As such, there is a reduced contribution from grain boundaries and other extrinsic factors, which often hinder ionic transport. Consequently, reported activation energies tend to be lower for μSR in comparison to other techniques, as μSR probes the fundamental energy required to motivate singular ionic hops at a unit cell length-scale.[37,47]

Within rhombohedral LZP, Li^+ is distributed over six disordered 36f tetrahedral sites surrounding the 6b site (Figure 4).[21] The chemical configuration of the Li sites is relatively unstable due to a distortion of their tetrahedral environment through a lengthening of the Li−O bond: an increase to 2.27 from 2.09 Å in comparison with the triclinic ($C\bar{1}$) phase. The distorted tetrahedral environment of Li^+ benefits mobility because of its inherent instability, and affords structural reasoning for ease of hopping between vacant 36f sites. The length of the Li−O bond depends on the cation used.[60] Structurally, the replacement of Ti for Zr reduces the bottleneck in the Li^+ conduction channel between the M1 and M2 sites (6b and 18e, respectively). This corresponds to the observed reduction in temperature required to motivate spontaneous diffusion.[25,61]

To deduce the diffusion coefficient of Li^+ ions, D_{Li}, the following equation was applied:

$$D_{Li} = \sum_{i=1}^{n} (1/N_i) Z_{\nu,i} s_i^2 \nu_{Li} \quad (2)$$

N_i is the number of Li^+ sites in the ith path, $Z_{\nu,i}$ is the vacancy fraction, s_i is the Li^+ hopping distance, and ν is the field fluctuation rate obtained via μSR.[34,40,56] There are two established mechanisms of Li^+ hopping: vacancy assisted and

https://dx.doi.org/10.1021/acsaem.0c02722
ACS Appl. Energy Mater. 2021, 4, 1527−1536

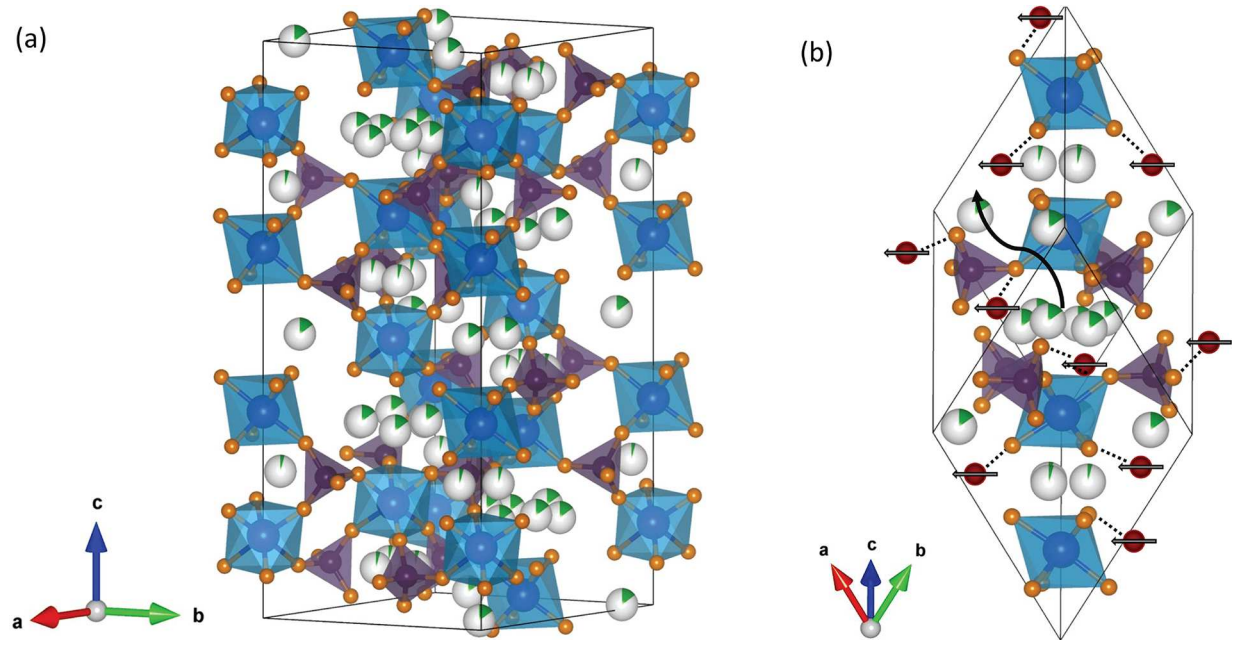

Figure 4. (a) Unit cell of rhombohedral ($R\bar{3}c$) LZP.[59] Li is displayed as green spheres in tetrahedral sites with a high vacancy fraction, Zr as blue, P as purple, and O as orange. ZrO_6 and PO_4 are shown as blue octahedra and purple tetrahedra, respectively. (b) View of LZP with rhombohedral axes. The curved black arrow indicates the Li^+ diffusion pathway from the 6b site surrounded by six split 36f Wyckoff positions to the neighboring 6b site. The dark red spheres indicate implanted muons, which are known to chemically bond to oxygen atoms at a distance of around 1 Å.[33,55] The muon spins are all facing the same direction, as is the case upon initial implantation. The potential muon stopping sites shown here are displayed for qualitative purposes only, while further information on potential muon stopping sites can be found in Tables S1−S6.

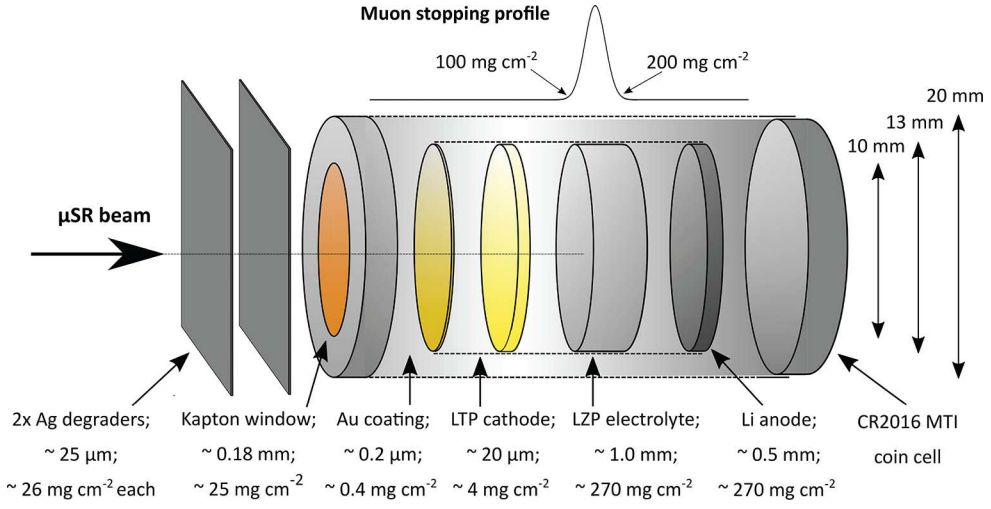

Figure 5. Labeled schematic of the Li|LZP|LTP cell as measured on the beamline. The battery constituents were assembled within a CR2016 MTI coin cell. The thickness of each component is given, along with an areal density, which is used to determine the amount of beam attenuation. The muon stopping profile is shown as a Gaussian distribution between around 100−200 mg cm^{-2}; muons, which enter through the 10 mm diameter Kapton inspection window, are predicted to come to rest within the LZP solid electrolyte.

interstitial. Lu et al. have shown the importance of interstitial sites at elevated temperatures for LTP, and that close to room temperature Li^+ opts to remain at the thermodynamically stable 6b sites.[32] The pathway considered for D_{Li} is thus from the 6b sites to the 6b sites via vacancy assisted hopping. For both materials, there are six potential pathways if we consider three-dimensional diffusivity. The hopping distances were taken from 6b to 6b sites at the center of the 36f Wyckoff positions from the recent studies by Noda et al.[19] and Lu et al.[32] for LZP and LTP, respectively. Noda et al. have shown that Li^+ migration proceeds via a pushing-out and repulsion mechanism, whereby a diffusing Li^+ pushes out another Li^+ occupying a 6b site, encouraging it to also diffuse. It is, therefore, assumed that every 6b site is available for diffusion and that Z is 1.

The diffusion coefficient, D_{Li}, of the electrolyte LZP and cathode LTP were estimated as 3.7 (2) × 10^{-10} and 6.9 (6) × 10^{-10} cm^2 s^{-1} at 336 K [5.1 (3) × 10^{-10} cm^2 s^{-1} at 297 K for LTP], respectively. Data at 336 K was used for LZP to ensure that the material had fully transitioned to the rhombohedral phase. LTP is seen to display slightly faster dynamics than LZP, as expected. This can be rationalized by the increased

https://dx.doi.org/10.1021/acsaem.0c02722
ACS Appl. Energy Mater. 2021, 4, 1527−1536

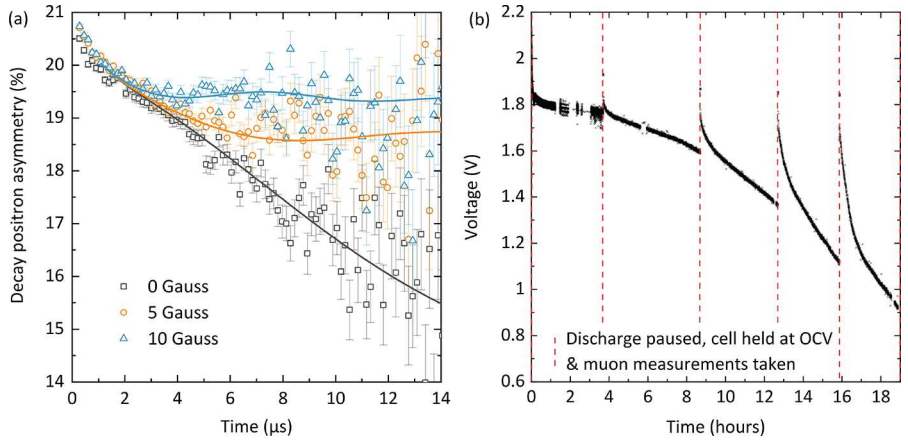

Figure 6. (a) Raw μSR data from the electrolyte LZP within the all-solid-state cell at 345 K, showing the reduced depolarization as the applied field increases. (b) Discharge profile of the Li|LZP|LTP cell at 8 μA cm^{-2}; the dotted lines show points at which the cell relaxed for 2 h 40 min to OCV and μSR and EIS measurements were performed. The discharge corresponds to a capacity of around 30 mAh g^{-1}. Further characterization of the solid-state cell configuration can be found in ref 15.

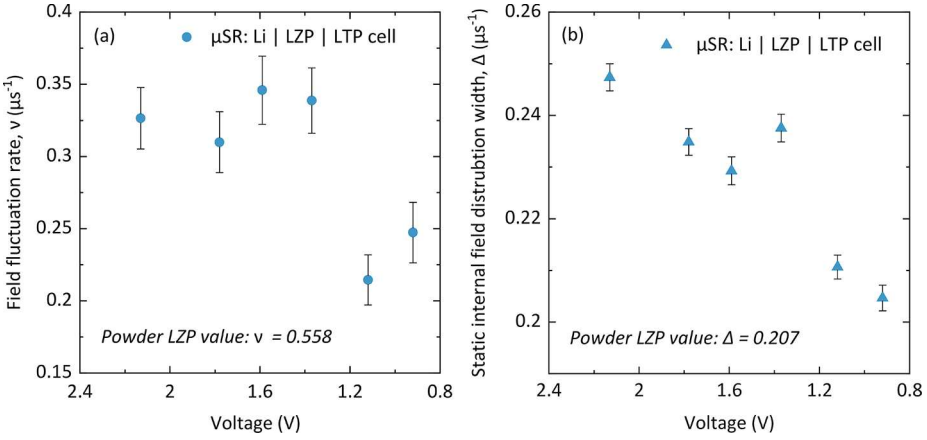

Figure 7. μSR measurements displaying (a) the field fluctuation rate ν and (b) the static field distribution width Δ as a function of discharge state of the Li|LZP|LTP cell. The values for the pristine LZP powder at 345 K are given in μs^{-1}.

width of the M1-M2 bottleneck which is known to hinder diffusion. Subramanian et al. showed that the substitution of Ti^{4+} for Zr^{4+} decreased both the *a* and *c* cell parameters significantly, shortening the diffusion pathway and increasing cavity size to afford greater Li^+ mobility.[31]

All-Solid-State Li|LZP|LTP Cell. As was recently reported, LTP and LZP can be cosintered together and a Li anode attached to form an all-solid-state cell.[15] A typical discharge/charge profile for this configuration displays an electrochemical window between 1.0−3.5 V. The beam penetration depth is a Gaussian distribution roughly between 100−200 mg cm^{-2} as an areal density. Accounting for a small amount of beam attenuation by the Kapton window and assuming a negligible affect from the thin (∼20 μm) cathode layer,[15] muons were predicted to stop with a range between 0.09−0.47 mm deep inside the 1.0 mm thick pellet (Figure 5). The μSR signal received was thus from the solid electrolyte itself. Zero and longitudinal field muon measurements were taken at six distinct discharge voltages, at which points the discharge was paused and the cell was allowed to relax for around 2 h and 40 min to open circuit voltage (OCV). Data were again fit using eq 1 in the time range 1−25 μs. The entire setup was held at 345 K to ensure that the solid electrolyte LZP existed in purely the fast-conducting rhombohedral phase. A low current density of 8 μA cm^{-2} was applied for the discharge, which is shown in Figure 6.

Figure 7a reflects how the Li^+ dynamics within the solid LZP electrolyte change depending on cell potential. The values obtained for ν and Δ in comparison to the powder LZP sample are similar and rationalize that the signal was collected from the electrolyte LZP within the cell. The field fluctuation rate ν is expected to stay constant within the inert solid electrolyte as the battery discharges, as it acts as a medium for ionic transfer. The following is observed: ν remains relatively constant as the cell is discharged until around 1.2 V below which there is a sharp drop in magnitude. The reduction in the rate of Li^+ diffusion in the electrolyte evidence a degree of instability at deep discharge of the battery (≤1.2 V). The low current density applied here is not expected to damage the electrolyte significantly over one discharge and thus the reduction in intrinsic self-diffusion at low temperatures is attributed to electrolyte instability at low electrochemical potential.[15,17] Using the same calculation method as in the previous section, D_{Li} is observed to decrease from an average of 2.2 (2) × 10^{-10} above 1.2 V to an average value of 1.6 (1) × 10^{-10} cm^2 s^{-1} below. These results demonstrate the sensitivity of this in situ muon technique in assessing ion transport properties under

https://dx.doi.org/10.1021/acsaem.0c02722
ACS Appl. Energy Mater. 2021, 4, 1527−1536

working conditions and at extreme conditions where instabilities become apparent.

Δ is observed to fluctuate slightly with a general decreasing trend which becomes more pronounced below 1.2 V. This suggests a changing spatial distribution of nuclear dipole fields near the muon site as the muon site itself is unlikely to change with voltage state. Since the Li content within the electrolyte is independent of the state of charge of the cell, it follows that Δ would be predicted to remain constant during cycling. The change in Δ may be caused by a narrowing of the bottleneck along the 6b−6b diffusion pathway between the 18e (M2) sites through a structural distortion of the Zr−O octahedra and P−O tetrahedra. The mechanism of attempting to extract excess Li^+ into lithiated LTP at a low potential may drive ions into the vacant 18e (M2) sites, hampering potential diffusion pathways between 6b sites and lowering the width of the field distribution felt by the implanted muons. The reduction in Δ may also be due to the decomposition of LZP at low potential. The magnitude of the reduction is comparable to a structural change, however the structural evolution of LZP at deep discharge has not yet been determined.

Along with muon measurements at each stopping point in the discharge cycle, electrochemical impedance spectroscopy (EIS) measurements were also taken in order to provide complementary information to the local diffusion probed by μSR. The overall cell resistance is seen to increase steadily from around 51 kΩ cm^2 before discharge to around 74 kΩ cm^2 at deep discharge (0.92 V) (Figure 8). The spectra shown are

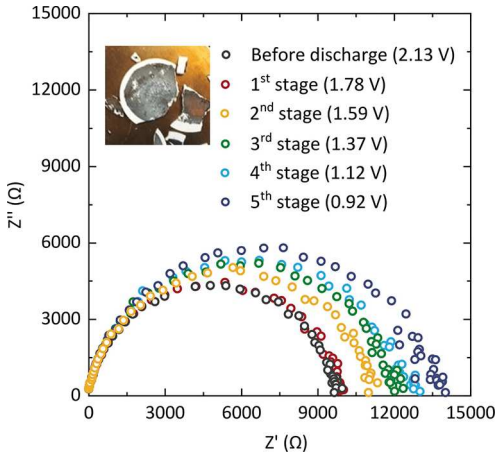

Figure 8. EIS measurement at each OCV voltage in the first discharge of the Li|LZP|LTP cell. The inset shows the Li/LZP black interfacial layer on a broken LZP pellet.

dominated by one large resistive effect in the battery which is likely to be the Li/LZP interfacial layer.[15] LZP reacts with metallic Li to form a black, amorphous, passivating layer, which has been reported to consist of Li_3P and Li_8ZrO_6 (the interphase is pictured in the inset of Figure 8).[15,17] X-ray absorption spectroscopy experiments reveal that the interphase can be propagated using either applied heat or current and that there is a clear change during interphase growth as the pristine material is converted to an amorphous material. XANES measurements find a shift in edge position which indicates a small change in the local structure (Figures S7−S11), while the EXAFS data displays a significant reduction in the Zr−O coordination number from the pristine material to the interphase.

The shift of the EIS peak of the semicircle to higher time constants as the cell discharges is thus attributed to an interphase growth which acts as an increasingly resistive boundary. The resistive component from the LZP/LTP interface is indistinguishable from the total resistance in the EIS spectra, suggesting the resistance across the all-NASICON boundary is substantially less. While the interface is essential to wet both LZP and Li and maintain stability across both components, the resistive increase observed over the first discharge will impede charge transfer across the boundary and consume active material. Interfacial resistance growth is not expected to contribute toward the reduced self-diffusion observed within the bulk at low potential; however, over extended cycling, it will lead to an inhomogeneous current distribution and ultimately a short-circuit.

CONCLUSIONS

Activation energies of LZP and LTP have been estimated as 51 ± 8 and 63 ± 6 meV, respectively. From this, the diffusion rate coefficient was estimated as 3.7 (2) × 10^{-10} and 6.9 (6) × 10^{-10} cm^2 s^{-1} at 336 K for LZP and LTP, respectively, and as 5.1 (3) × 10^{-10} cm^2 s^{-1} at room temperature for LTP. Both NASICON materials exhibit low energetic barriers for Li^+ hopping and fast ion mobility, while LTP displays faster transport due to the smaller effective ionic radius of Ti^{4+} easing the bottleneck restriction on the M1-M2-M1 diffusion pathway. μSR results for a NASICON-structured Li|LZP|LTP SSB displayed a drop in the Li^+ diffusion rate below ≤1.2 V, indicating ionic conductivity is significantly hindered at deep discharge. A reduction in the static field distribution width with discharge reveals potential structural distortion which may be the cause of the reduced hopping rate by a narrowing of the diffusion pathway between M1 sites. The correlated reduction in both ν and Δ indicates that LZP may undergo structural decomposition at low voltage. Electrochemical impedance spectroscopy indicates the Li/LZP interfacial layer is the dominant resistive barrier within the cell and becomes increasingly resistive throughout the first discharge. This work offers an initial insight into the applicability of in situ μSR and electrochemical techniques as a combined tool to investigate energy storage devices by elucidating the relationship between diffusional properties and electrochemistry. The technique can be applied to study of the behavior of a singular battery component or a whole device and can be extended toward the study of interfacial regions and degradation mechanisms.[47] In situ cell design improvements to further develop this technique are underway to optimize data quality, electrochemistry, and cell assembly.

ASSOCIATED CONTENT

Supporting Information

The Supporting Information is available free of charge at https://pubs.acs.org/doi/10.1021/acsaem.0c02722.

Fitted muon spin relaxation data and also further characterization of the parent materials using X-ray diffraction, scanning electron microscopy, and X-ray absorption spectroscopy (PDF)

AUTHOR INFORMATION

Corresponding Author

Serena A. Corr − *Department of Chemical and Biological Engineering, The University of Sheffield, Sheffield S1 3JD,*

https://dx.doi.org/10.1021/acsaem.0c02722
ACS Appl. Energy Mater. 2021, 4, 1527−1536

U.K.; orcid.org/0000-0002-9303-4220; Email: s.corr@sheffield.ac.uk

Authors

Innes McClelland − *Department of Chemical and Biological Engineering, The University of Sheffield, Sheffield S1 3JD, U.K.; ISIS Neutron and Muon Source, Science and Technology Facilities Council, Rutherford Appleton Laboratory, Didcot OX11 0QX, U.K.; The Faraday Institution, Didcot OX11 0RA, U.K.;* orcid.org/0000-0001-9821-715X

Samuel G. Booth − *Department of Chemical and Biological Engineering, The University of Sheffield, Sheffield S1 3JD, U.K.; The Faraday Institution, Didcot OX11 0RA, U.K.;* orcid.org/0000-0001-7643-4196

Hany El-Shinawi − *Department of Chemical and Biological Engineering, The University of Sheffield, Sheffield S1 3JD, U.K.; The Faraday Institution, Didcot OX11 0RA, U.K.;* orcid.org/0000-0002-4743-5576

Beth I. J. Johnston − *Department of Chemical and Biological Engineering, The University of Sheffield, Sheffield S1 3JD, U.K.; The Faraday Institution, Didcot OX11 0RA, U.K.;* orcid.org/0000-0002-3586-1682

Jasmin Clough − *Department of Materials Science and Engineering, The University of Sheffield, Sheffield S1 3JD, U.K.; The Faraday Institution, Didcot OX11 0RA, U.K.*

Weimin Guo − *Department of Chemical and Biological Engineering, The University of Sheffield, Sheffield S1 3JD, U.K.*

Edmund J. Cussen − *Department of Materials Science and Engineering, The University of Sheffield, Sheffield S1 3JD, U.K.; The Faraday Institution, Didcot OX11 0RA, U.K.;* orcid.org/0000-0002-2899-6888

Peter J. Baker − *ISIS Neutron and Muon Source, Science and Technology Facilities Council, Rutherford Appleton Laboratory, Didcot OX11 0QX, U.K.; The Faraday Institution, Didcot OX11 0RA, U.K.;* orcid.org/0000-0002-2306-2648

Complete contact information is available at: https://pubs.acs.org/10.1021/acsaem.0c02722

Notes

The authors declare no competing financial interest.

■ ACKNOWLEDGMENTS

The authors thank the ISIS Neutron and Muon facility, through the award of beamtime (DOI: 10.5286/ISIS.E.RB1820558), a Facility Development Studentship for IMC, and Josef Lewis and Jamie Nutter for enabling the in situ muon experiment. B.I.J. acknowledges the award of a Carnegie PhD scholarship. This work was supported by the EPSRC [EP/N001982/2], the ISCF Faraday Challenge projects SOLBAT [Grant FIRG007], and FutureCat [FIRG017]. We acknowledge SOLEIL for provision of synchrotron radiation facilities, and we would like to thank Stéphanie Belin for assistance in using the ROCK beamline, proposal number 20181039.

■ REFERENCES

(1) Ding, Y.; Cano, Z. P.; Yu, A.; Lu, J.; Chen, Z. Automotive Li-Ion Batteries: Current Status and Future Perspectives. *Electrochemical Energy Reviews* **2019**, *2*, 1−28.

(2) Fu, K.; Gong, Y.; Liu, B.; Zhu, Y.; Xu, S.; Yao, Y.; Luo, W.; Wang, C.; Lacey, S. D.; Dai, J.; Chen, Y.; Mo, Y.; Wachsman, E.; Hu, L. Toward garnet electrolyte-based Li metal batteries: An ultrathin, highly effective, artificial solid-state electrolyte/metallic Li interface. *Sci. Adv.* **2017**, *3*, No. e1601659.

(3) Zheng, F.; Kotobuki, M.; Song, S.; Lai, M. O.; Lu, L. Review on solid electrolytes for all-solid-state lithium-ion batteries. *J. Power Sources* **2018**, *389*, 198−213.

(4) Manthiram, A.; Yu, X.; Wang, S. Lithium battery chemistries enabled by solid-state electrolytes. *Nat. Rev. Mater.* **2017**, *2*, 16103.

(5) Liu, B.; Zhang, J. G.; Xu, W. Advancing Lithium Metal Batteries. *Joule* **2018**, *2*, 833−845.

(6) Wang, S.; Xu, H.; Li, W.; Dolocan, A.; Manthiram, A. Interfacial Chemistry in Solid-State Batteries: Formation of Interphase and Its Consequences. *J. Am. Chem. Soc.* **2018**, *140*, 250−257.

(7) Gao, Z.; Sun, H.; Fu, L.; Ye, F.; Zhang, Y.; Luo, W.; Huang, Y. Promises, Challenges, and Recent Progress of Inorganic Solid-State Electrolytes for All-Solid-State Lithium Batteries. *Adv. Mater.* **2018**, *30*, 1705702.

(8) Sun, C.; Liu, J.; Gong, Y.; Wilkinson, D.; Zhang, J. Recent advances in all-solid-state rechargeable lithium batteries. *Nano Energy* **2017**, *33*, 363−386.

(9) Famprikis, T.; Canepa, P.; Dawson, J. A.; Islam, M. S.; Masquelier, C. Fundamentals of inorganic solid-state electrolytes for batteries. *Nat. Mater.* **2019**, *18*, 1278−1291.

(10) Chung, H.; Kang, B. Mechanical and Thermal Failure Induced by Contact between a $Li_{1.5}Al_{0.5}Ge_{1.5}(PO_4)_3$ Solid Electrolyte and Li Metal in an All Solid-State Li Cell. *Chem. Mater.* **2017**, *29*, 8611−8619.

(11) Huo, H.; Liang, J.; Zhao, N.; Li, X.; Lin, X.; Zhao, Y.; Adair, K.; Li, R.; Guo, X.; Sun, X. Dynamics of the Garnet/Li Interface for Dendrite-Free Solid-State Batteries. *ACS Energy Lett.* **2020**, *5*, 2156−2164.

(12) Li, G.; Monroe, C. Dendrite nucleation in lithium-conductive ceramics. *Phys. Chem. Chem. Phys.* **2019**, *21*, 20354−20359.

(13) Yamada, H.; Ito, T.; Basappa, R. H.; Bekarevich, R.; et al. Influence of strain on local structure and lithium ionic conduction in garnet-type solid electrolyte. *J. Power Sources* **2017**, *368*, 97−106.

(14) Flatscher, F.; Philipp, M.; Ganschow, S.; Wilkening, H. M. R.; Rettenwander, D. The natural critical current density limit for $Li_7La_3Zr_2O_{12}$ garnets. *J. Mater. Chem. A* **2020**, *8*, 15782−15788.

(15) El-Shinawi, H.; Regoutz, A.; Payne, D. J.; Cussen, E. J.; Corr, S. A. NASICON $LiM_2(PO_4)_3$ electrolyte (M = Zr) and electrode (M = Ti) materials for all solid-state Li-ion batteries with high total conductivity and low interfacial resistance. *J. Mater. Chem. A* **2018**, *6*, 5296−5303.

(16) O'Rourke, C.; Morgan, B. Interfacial strain effects on lithium diffusion pathways in the spinel solid electrolyte Li-doped $MgAl_2O_4$. *Phys. Rev. Mater.* **2018**, *2*, 045043.

(17) Li, Y.; Zhou, W.; Chen, X.; Lü, X.; Cui, Z.; Xin, S.; Xue, L.; Jia, Q.; Goodenough, J. B. Mastering the interface for advanced all-solid-state lithium rechargeable batteries. *Proc. Natl. Acad. Sci. U. S. A.* **2016**, *113*, 13313−13317.

(18) Andriiko, A. A.; Rudenok, P. V.; Nyrkova, L. I. Diffusion coefficient of Li^+ in solid-state rechargeable battery materials. *J. Power Sources* **1998**, *72*, 146−149.

(19) Noda, Y.; Nakano, K.; Takeda, H.; Kotobuki, M.; Lu, L.; Nakayama, M. Computational and Experimental Investigation of the Electrochemical Stability and Li-Ion Conduction Mechanism of $LiZr_2(PO_4)_3$. *Chem. Mater.* **2017**, *29*, 8983−8991.

(20) Zhang, J.; Zhang, J.; Ou, X.; Wang, C.; Peng, C.; Zhang, B. Enhancing High-Voltage Performance of Ni-Rich Cathode by Surface Modification of Self-Assembled NASICON Fast Ionic Conductor $LiZr_2(PO_4)_3$. *ACS Appl. Mater. Interfaces* **2019**, *11*, 15507−15516.

(21) Catti, M.; Stramare, S.; Ibberson, R. Lithium location in NASICON-type Li^+ conductors by neutron diffraction. I. Triclinic α'-$LiZr_2(PO_4)_3$. *Solid State Ionics* **1999**, *123*, 173−180.

(22) Rossbach, A.; Tietz, F.; Grieshammer, S. Structural and transport properties of lithium-conducting NASICON materials. *J. Power Sources* **2018**, *391*, 1−9.
(23) Meesala, Y.; Jena, A.; Chang, H.; Liu, R. S. Recent Advancements in Li-Ion Conductors for All-Solid-State Li-Ion Batteries. *ACS Energy Lett.* **2017**, *2*, 2734−2751.
(24) Ramar, V.; Kumar, S.; Sivakkumar, S. R.; Balaya, P. NASICON-type La^{3+} substituted $LiZr_2(PO_4)_3$ with improved ionic conductivity as solid electrolyte. *Electrochim. Acta* **2018**, *271*, 120−126.
(25) Hou, M.; Liang, F.; Chen, K.; Dai, Y.; Xue, D. Challenges and perspectives of NASICON-type solid electrolytes for all-solid-state lithium batteries. *Nanotechnology* **2020**, *31*, 132003.
(26) Pareek, T.; Dwivedi, S.; Singh, B.; Kumar, D.; Kumar, P.; Kumar, S. $LiSnZr(PO_4)_3$: NASICON-type solid electrolyte with excellent room temperature Li^+ conductivity. *J. Alloys Compd.* **2019**, *777*, 602−611.
(27) Xie, H.; Goodenough, J. B.; Li, Y. $Li_{1.2}Zr_{1.9}Ca_{0.1}(PO_4)_3$, a room-temperature Li-ion solid electrolyte. *J. Power Sources* **2011**, *196*, 7760−7762.
(28) Zhang, Y.; Chen, K.; Shen, Y.; Lin, Y.; Nan, C. W. Enhanced lithium-ion conductivity in a $LiZr_2(PO_4)_3$ solid electrolyte by Al doping. *Ceram. Int.* **2017**, *43*, S598−S602.
(29) Hartmann, P.; Leichtweiss, T.; Busche, M.; Schneider, M.; Reich, M.; Sann, J.; Adelhelm, P.; Janek, J. Degradation of NASICON-Type Materials in Contact with Lithium Metal: Formation of Mixed Conducting Interphases (MCI) on Solid Electrolytes. *J. Phys. Chem. C* **2013**, *117*, 21064−21074.
(30) Cassel, A.; Fleutot, B.; Courty, M.; Viallet, V.; Morcrette, M. Sol-gel synthesis and electrochemical properties extracted by phase inflection detection method of NASICON-type solid electrolytes $LiZr_2(PO_4)_3$ and $Li_{1.2}Zr_{1.9}Ca_{0.1}(PO_4)_3$. *Solid State Ionics* **2017**, *309*, 63−70.
(31) Subramanian, M. A.; Subramanian, R.; Clearfield, A. Lithium ion conductors in the system $AB(IV)_2(PO_4)_3$ (B = Ti, Zr and Hf). *Solid State Ionics* **1986**, *18*−*19*, 562−569.
(32) Lu, X.; Wang, S.; Xiao, R.; Shi, S.; Li, H.; Chen, L. First-principles insight into the structural fundamental of super ionic conducting in NASICON $MTi_2(PO_4)_3$ (M = Li, Na) materials for rechargeable batteries. *Nano Energy* **2017**, *41*, 626−633.
(33) Blundell, S. J. Spin-polarized muons in condensed matter physics. *Contemp. Phys.* **1999**, *40*, 175−192.
(34) Sugiyama, J.; Mukai, K.; Ikedo, Y.; Nozaki, H.; Månsson, M.; Watanabe, I. Li Diffusion in Li_xCoO_2 Probed by Muon-Spin Spectroscopy. *Phys. Rev. Lett.* **2009**, *103*, 147601.
(35) Ashton, T. E.; Laveda, J. V.; Maclaren, D. A.; Baker, P. J.; Porch, A.; Jones, M. O.; Corr, S. A. Muon studies of Li^+ diffusion in $LiFePO_4$ nanoparticles of different polymorphs. *J. Mater. Chem. A* **2014**, *2*, 6238−6245.
(36) Laveda, J. V.; Johnston, B.; Paterson, G. W.; Baker, P. J.; Tucker, M. G.; Playford, H. Y.; Jensen, K. M. Ø.; Billinge, S. J. L.; Corr, S. A. Structure-property insights into nanostructured electrodes for Li-ion batteries from local structural and diffusional probes. *J. Mater. Chem. A* **2018**, *6*, 127−137.
(37) Baker, P. J.; Franke, I.; Pratt, F. L.; Lancaster, T.; Prabhakaran, D.; Hayes, W.; Blundell, S. J. Probing magnetic order in $LiMPO_4$ (M = Ni, Co, Fe) and lithium diffusion in Li_xFePO_4. *Phys. Rev. B: Condens. Matter Mater. Phys.* **2011**, *84*, 174403.
(38) Johnson, I. D.; Ashton, T. E.; Blagovidova, E.; Smales, G. J.; Lübke, M.; Baker, P. J.; Corr, S. A.; Darr, J. A. Mechanistic insights of Li_+ diffusion within doped $LiFePO_4$ from Muon Spectroscopy. *Sci. Rep.* **2018**, *8*, 4114.
(39) Månsson, M.; Nozaki, H.; Wikberg, J. M.; Prša, K.; Sassa, Y.; Dahbi, M.; Kamazawa, K.; Sedlak, K.; Watanabe, I.; Sugiyama, J. Lithium diffusion & magnetism in battery cathode material $Li_xNi_{1/3}Co_{1/3}Mn_{1/3}O_2$. *J. Phys. Conf. Ser.* **2014**, *551*, 012037.
(40) Månsson, M.; Sugiyama, J. Muon-spin relaxation study on Li- and Na-diffusion in solids. *Phys. Scr.* **2013**, *88*, 068509.
(41) Umegaki, I.; Kawauchi, S.; Sawada, H.; Nozaki, H.; Higuchi, Y.; Miwa, K.; Kondo, Y.; Månsson, M.; Telling, M.; Coomer, F. C.; Cottrell, S. P.; Sasaki, T.; Kobayashi, T.; Sugiyama, J. Li-ion diffusion in Li intercalated graphite C_6Li and $C_{12}Li$ probed by μ^+SR. *Phys. Chem. Chem. Phys.* **2017**, *19*, 19058−19066.
(42) Sugiyama, J.; Nozaki, H.; Umegaki, I.; Mukai, K.; Miwa, K.; Shiraki, S.; Hitosugi, T.; Suter, A.; Prokscha, T.; Salman, Z.; Lord, J. S.; Månsson, M. Li-ion diffusion in $Li_4Ti_5O_{12}$ and $LiTi_2O_4$ battery materials detected by muon spin spectroscopy. *Phys. Rev. B: Condens. Matter Mater. Phys.* **2015**, *92*, 014417.
(43) Powell, A. S.; Lord, J. S.; Gregory, D. H.; Titman, J. J. Muon Spin Relaxation Studies of Lithium Nitridometallate Battery Materials: Muon Trapping and Lithium Ion Diffusion. *J. Phys. Chem. C* **2009**, *113*, 20758−20763.
(44) Ferdani, D. W.; Pering, S. R.; Ghosh, D.; Kubiak, P.; Walker, A. B.; Lewis, S. E.; Johnson, A. L.; Baker, P. J.; Islam, M. S.; Cameron, P. J. Partial cation substitution reduces iodide ion transport in lead iodide perovskite solar cells. *Energy Environ. Sci.* **2019**, *12*, 2264−2272.
(45) Amores, M.; Baker, P. J.; Cussen, E. J.; Corr, S. A. $Na_{1.5}La_{1.5}TeO_6$: Na^+ conduction in a novel Na-rich double perovskite. *Chem. Commun.* **2018**, *54*, 10040−10043.
(46) Martin, D. Z. C.; Haworth, A. R.; Schmidt, W. L.; Baker, P. J.; Boston, R.; Johnston, K. E.; Reeves-McLaren, N. Evaluating lithium diffusion mechanisms in the complex spinel $Li_2NiGe_3O_8$. *Phys. Chem. Chem. Phys.* **2019**, *21*, 23111−23118.
(47) McClelland, I.; Johnston, B.; Baker, P. J.; Amores, M.; Cussen, E. J.; Corr, S. A. Muon Spectroscopy for Investigating Diffusion in Energy Storage Materials. *Annu. Rev. Mater. Res.* **2020**, *50*, 371.
(48) El-Shinawi, H.; Janek, J. Low-temperature synthesis of macroporous $LiTi_2(PO_4)_3$/C with superior lithium storage properties. *RSC Adv.* **2015**, *5*, 14887−14891.
(49) Momma, K.; Izumi, F. VESTA 3 for three-dimensional visualization of crystal, volumetric and morphology data. *J. Appl. Crystallogr.* **2011**, *44*, 1272−1276.
(50) Arnold, O.; et al. Mantid - Data analysis and visualization package for neutron scattering and μSR experiments. *Nucl. Instrum. Methods Phys. Res., Sect. A* **2014**, *764*, 156−166.
(51) Keren, A. Generalization of the Abragam relaxation function to a longitudinal field. *Phys. Rev. B: Condens. Matter Mater. Phys.* **1994**, *50*, 10039−10042.
(52) Hayano, R. S.; Uemura, Y. J.; Imazato, J.; Nishida, N.; Yamazaki, T.; Kubo, R. Zero-and low-field spin relaxation studied by positive muons. *Phys. Rev. B: Condens. Matter Mater. Phys.* **1979**, *20*, 850−859.
(53) Sugiyama, J.; Nozaki, H.; Umegaki, I.; Mukai, K.; Cottrell, S. P.; Shiraki, S.; Hitosugi, T.; Sassa, Y.; Suter, A.; Salman, Z.; Prokscha, T.; Månsson, M.; et al. μ^+SR Study on Li Ionic Conductors. *JPS Conf. Proc.* **2017**, *21*, 14−17.
(54) Stone, N. J. Table of nuclear magnetic dipole and electric quadrupole moments. *At. Data Nucl. Data Tables* **2005**, *90*, 75−176.
(55) Holzschuh, E.; Denison, A. B.; Kündig, W.; Meier, P. F.; Patterson, B. D. Muon-spin-rotation experiments in orthoferrites. *Phys. Rev. B: Condens. Matter Mater. Phys.* **1983**, *27*, 5294−5307.
(56) Amores, M.; Ashton, T. E.; Baker, P. J.; Cussen, E. J.; Corr, S. A. Fast microwave-assisted synthesis of Li-stuffed garnets and insights into Li diffusion from muon spin spectroscopy. *J. Mater. Chem. A* **2016**, *4*, 1729−1736.
(57) Nozaki, H.; Harada, M.; Ohta, S.; Watanabe, I.; Miyake, Y.; Ikedo, Y.; Jalarvo, N. H.; Mamontov, E.; Sugiyama, J. Li diffusive behavior of garnet-type oxides studied by muon-spin relaxation and QENS. *Solid State Ionics* **2014**, *262*, 585−588.
(58) Sugiyama, J.; Mukai, K.; Nozaki, H.; Harada, M.; Kamazawa, K.; Ikedo, Y.; Månsson, M.; Ofer, O.; Ansaldo, E. J.; Brewer, J. H.; Chow, K. H.; Watanabe, I.; Miyake, Y.; Ohzuku, T. Lithium Diffusion in Lithium-Transition-Metal Oxides Detected by μ^+SR. *Phys. Procedia* **2012**, *30*, 105−108.
(59) Catti, M.; Comotti, A.; Di Blas, S. High-Temperature Lithium Mobility in α-$LiZr_2(PO_4)_3$ NASICON by Neutron Diffraction. *Chem. Mater.* **2003**, *15*, 1628−1632.

https://dx.doi.org/10.1021/acsaem.0c02722
ACS Appl. Energy Mater. 2021, 4, 1527−1536

(60) Aatiq, A.; Ménétrier, M.; Croguennec, L.; Suard, E.; Delmas, C. On the structure of $Li_3Ti_2(PO_4)_3$. *J. Mater. Chem.* **2002**, *12*, 2971−2978.
(61) Martínez-Juárez, A.; Pecharromán, C.; Iglesias, J. E.; Rojo, J. M. Relationship between activation energy and bottleneck size for Li^+ ion conduction in NASICON materials of composition $LiMM'(PO_4)_3$; M, M′ = Ge, Ti, Sn, Hf. *J. Phys. Chem. B* **1998**, *102*, 372−375.

https://dx.doi.org/10.1021/acsaem.0c02722
ACS Appl. Energy Mater. 2021, 4, 1527−1536